CHAPTER 2

THEORIES

2.1 Exoplanet

Exoplanets are planets outside of the solar system. The first exoplanets are discovered in 1992 (Wolszczan and Frail, 1992). Nowadays, astronomers discovered more than 1900 planetary systems. Most of planets which have been discovered are not similar to the Earth but similar to Jupiter or Neptune as giant gas planets.

Fewer than 5 percent of known exoplanets can be observed directly with telescopes. Therefore, astronomers have created techniques to find exoplanets. Currently, the most common method is the transit method. Around 1200 (as in 2015) exoplanets were discovered by this technique. Transit method is a method which looks for a periodic dip in the stellar light curve when a planet passes in front of its host star in the direction of the observer line-of-sight. The star flux temporarily decreases since it is blocked by the planet. From transit observations, planetary orbital parameters and physical parameters of the planet are obtained.

Another way to identify an exoplanet is Doppler spectroscopy. It uses radial velocity measurements through surveying Doppler shifts in the spectrum of a star due to its orbital motion. Astronomers look for a small change in radial velocity of a star by tracking its change overtime. Astronomers can estimate the mass of planet. In addition, some astronomers use astrometric technique to detect the position of a star in the sky and see how it makes small changes of position, which could indicate a planet nearby. In addition (as on September 2015)[1], 40 exoplanets were discovered by gravitational microlensing, 61 exoplanets were discovered by direct imaging and 19 exoplanets were discovered by pulsar timing.

[1] http://exoplanet.eu

NASA suggests the volume of space that would be explore is limited to the closest stars. Using technologies available in the next decade, space scientists will be able to explore stars that lie within approximately 20 parsecs (60 light-years) from the sun. There are some evidence that exoplanet systems resemble to the solar system will be found. Recent discovery showed that the star 55 Cancri (Marcy and Butler, 1998), 41 light-year away, contain 9 planets with distributions somewhat similar to the solar system's inner planet (though with much higher masses). Recently, astronomers discovered the first Earth-size planet orbiting a star in the habitable zone by using NASA's Kepler space telescope. The discovered of Kepler-186f (Quintana et al., 2014) confirms that planet with the size of the Earth exist in the habitable zone of star other than our sun.

2.2 Methods for Detection

Exoplanet is difficult to detect, because it has low mass and very faint comparing to its host star. Nowadays, various techniques used to detect exoplanets have been developed. There are methods relatively high resolution consists of radial velocity, gravitational microlensing, direct imaging, pulsar timing and transit methods.

2.2.1 Transit Method

Transit technique bases on the observation of small drop in brightness of a star. When a planet passes between the observer and its host star, planet blocks some of the light of star during the transit and create a periodic dip in the brightness of the star. From transit observation, orbital parameters of planetary system and physical parameters of the planet are obtained, such as radius. This method could not apply to every systems, because only about 10% of Jovian planet are aligned in such a way that observer see the planet's transit. Smaller planets in larger orbits are even less likely to be aligned in such a way that observer can observe the transit. The first exoplanet discovered by this method is HD 209458b (Charbonneau et al., 2000) (Figure 2.1). Nowadays, over 1200 exoplanets were discovered by this method.

Transit technique searches can operate on a large proportion. Detections of exo-planet have been discovered using the transit method though ground based searches such as TrEs, OGLE, HAT and WASP, and space based searches such as Kepler, At present, Kepler mission has discovered more than 1000 planets, which show signs of transits.

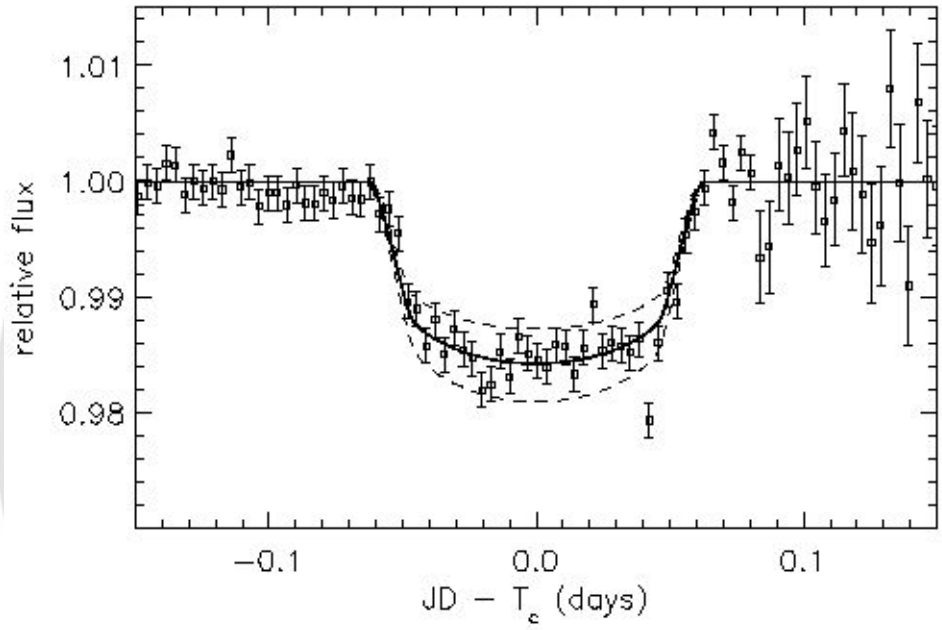

Figure 2.1: Light curves of star HD 209458 (Charbonneau et al., 2000).

2.2.2 Radial velocity method

Radial velocity is a technique which looks for the periodic Doppler shifts in the star's spectral lines as the star orbit around the center of mass due to the gravitational interaction with other planets. Stellar spectral lines move periodically redward or blueward due to the Doppler shift. This method is suitable for a planet with short period due to the higher amplitude of signal radial velocity, K_*. The amplitude of radial velocity signal of a stellar mass, M_*, and a planet mass, M_p, orbiting around with period, P_p, is given by

$$K_* = \frac{M_p \sin i_p}{M_*} \cdot \frac{2\pi a_p}{P_p}. \tag{2.1}$$

where i_p is the orbital inclination and a_p is the planet separation. The observed parameters are used to calculate a minimum mass which can use to measure the actual mass of a planet.

The radial velocity method is the first successful method for the detection of exoplanet, and is responsible for analyzing distanced exoplanets. It is the effective method for detecting exoplanets from Earth. During the past decade, this technique have been used to detect gas giant planet in Jupiter-like orbits. 51Peg b is the first exoplanet detected and confirmed by this method (Mayor and Queloz, 1995) (Figure 2.2).

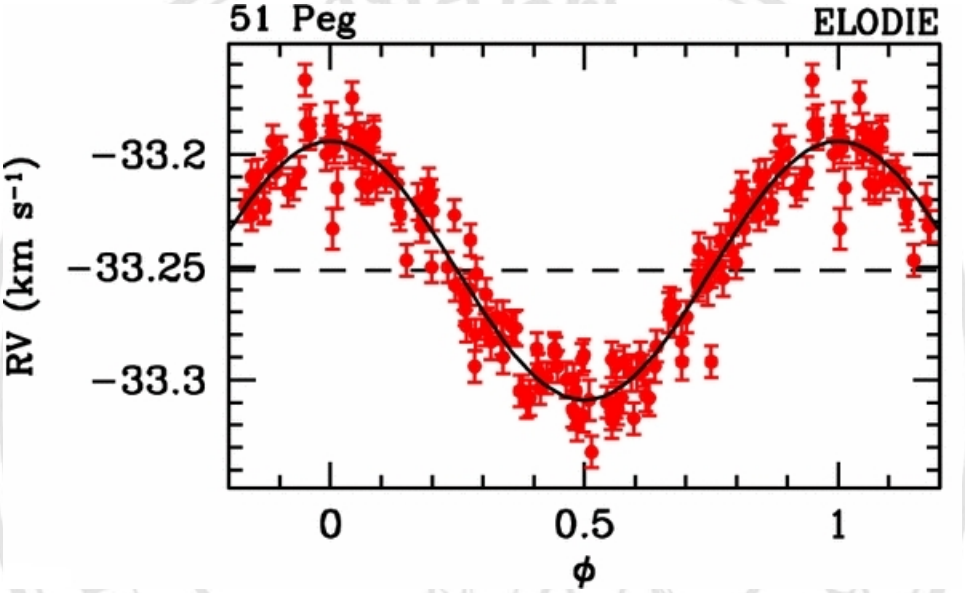

Figure 2.2: Radial Velocity of 51 Peg (Mayor and Queloz, 1995).

2.2.3 Gravitational microlensing method

Gravitational microlensing is an astronomical phenomenon of occurrence due to the effect of gravitational lenses. It can be used to detect planets or stars, regardless of their emission light. Generally, astronomers can detect only object which emits light (star) or large object that block light of background (such as gas and dust clouds). These object are only a small part of the galaxy. However, microlensing technique can be used to study objects that emit little or no light at all.

A distant star or quasar obtains sufficiently aligned with a massive compact foreground object, its light was bended due to the foreground gravitational field, as discussed in 1915 by Einstein. He predicted that the gravitational field can lead to distortion of observed image. Shape of microlensing light curve depends on mass of object that obscures

the front as well as the relative motion between background source and foreground lens.

The observed light curve from microlensing event does not depend on the radiation of lens star. Therefore, this phenomenon allows astronomers to study large mass object although its light is faint. This technique is an ideal technique for study the galactic population of object that faint or dark such as brown dwarfs, red dwarfs, neutron stars, planets, black holes, white dwarfs, and massive compact halo objects. Moreover, effect of microlensing event does not depend on the wavelength. Therefore, this technique can be used to study any source that emit any kind of electromagnetic radiation.

In 1993, the isolated object was first detected by microlensing technique (Kaiser and Squires, 1993) . Since then, this technique has been used to study the nature of dark matter, detect exoplanet, study limb darkening in distant stars, constrain the structure of the Milky way's disk and the binary star population.

2.2.4 Direct imaging method

Direct imaging method uses Infrared wavelengths to observe extrasolar planet directly, because, in Infrared wavelengths, a star like the sun is only 100 times brighter than Jupiter, comparing to a billion (10^9) times in visual wavelengths. This method is used to detect planet that orbit far from host star. However, in order to obtain planetary orbital properties, astronomers have to examine that the planet and the star move together through space to prove that the planets orbit around the star for hundreds or thousands year. This method cannot measure the mass of planet directly but can be used to obtain information about surface temperature and diameter of the planet from use the spectrum and brightness. The first exoplanet discovered by this method in 2008, which used visible light observations from telescope on Earth (Marois et al., 2008). Currently (as in 2015) there are 60 planets discovered by this method.

2.2.5 Pulsar Timing method

Pulsar timing method was first used to detect the exoplanet by Aleksander Wolszczan and Dale Frail in 1992. The first exoplanets to be discovered by this method are

PSR 1257+12B and PSR 1257+12C (Wolszczan and Frail, 1992). These exoplanets orbit a rapid rotating neutron star, which is called pulsar. A neutron star is the remnant of the collapse of a supernova explosion. When a neutron star rotate, it emits intensive electromagnetic radiation that is detected on Earth as regular and precisely timed pulses. Pulsars emit pulse radiation with periods ranging from milliseconds to several seconds, which depend on the rotation speed of the star. Slight regular variations in timing of pulses show that pulsar is orbiting around center of mass of system with one or more planets. Astronomers can estimate orbit and mass of extrasolar planet by precisely measuring deformation in the timing of the pulsars. This method is used the change of position of the pulsars, which is a result of gravitational interaction, which causes the change in distance and light-travel-time between pulsar and observer and establish the change in time of arrival. The method has high sensitivity which can be detected. However, pulsars are relatively rare celestial objects and from 1992 to 2015, only 19 extrasolar planets had been discovered by this method.

2.3 Transiting exoplanet surveys

Most exoplanets have been observed by using ground- based telescopes, but space telescope could do a better survey. Currently, there are several projects to search for exoplanets, whether ground-based search projects and space-based mission, such as HATNet, HATSouth, WASP, KELT, CoROT, and Kepler.

2.3.1 HATNet

The HATNet (Hungarian-made Automated Telescope Network) is a network of 6 small fully automated telescopes (4 at Fred Lawrence Whipple observatory, Arizona, and 2 at Mauna Kea, Hawaii) was established in 2003 (Bakos et al., 2004). The scientific goal of the project is to detect and characterize extrasolar planets using the transit method. The first transit exoplanet was discovered by HATNet is HAT-P-1b in 2006 (Bakos et al., 2007).

2.3.2 HATSouth

The HATSouth (Hungarian-made Automated Telescope Network-South) exoplanet survey is a network of 6 astrograph telescope systems designed to detect transiting exoplanet in orbit around relatively bright star visible from the southern hemisphere. The telescope were distributed over three continents; South America, Africa and Australia.

2.3.3 WASP

The WASP (Wide Angle Search for Planets) is the UK's leading exoplanet detection programme. It originally comprises a consortium of eight academics. The WASP consists of two robotic observatories. The first, superWASP-North is located on the island of La Palma amongst the Isaac Newton Group of telescope (ING). The second, superWASP-South is located at the site of the South African Astronomical Observatory (SAAO), South African. The observatories consist of eight wide-angle cameras that simultaneously monitor the sky for planetary transit event.

2.3.4 KELT

The Kilodegree Extremely Little Telescope (KELT) project is a survey for planetary transits of bright star. It consist of a small aperture, wide-field automated telescope located at Winer Observatory near Arizona. The telescope surveys is a set of $26^\circ \times 26^\circ$ fields that together cover about 25% of the northern sky, and targets star in the range of $8 < V < 10$ mag. This survey searches for transits by close-in Jupiter (Pepper et al., 2007).

2.3.4.1 CoRoT

The CoROT (Convention, Rotation and planetary Transits) is the first space mission dedicated to searching for exoplanets orbiting a short period and measurements of asteroseismology of variable stars. The spacecraft is equipped with a 27 cm-diameter focal telescope and 4 CCD wide-field cameras, and operates in a low-Earth orbit (LEO) of $\sim$ 900 km (polar) launched in December 2006. The first exoplanet detected by CoROT

is CoROT-1b in March, 2007 and the first transiting detected Super-Earth is CoROT-7b (Léger et al., 2009).

2.3.4.2 Kepler

The Kepler is a space observatory launched by NASA to discover Earth-like planets orbiting other stars. It was launched on March 7, 2009 and was equipped with a 0.95-m telescope with 42 CCDs (field of view of 105 deg^2). In 2011, the Kepler mission released data for 156,453 stars. In 2012, more than 1,000 additional candidates were announced (Batalha et al., 2013). In 2013, the discovery of 461 more candidates was announced on January 7, 2013. In January 2015. The number of planet was discovered by Kepler and confirmed to exceeded 1000 planets.

2.4 Transiting exoplanet

2.4.1 Characterizing transiting exoplanet

The transit method is based on the observation of a small drop in brightness of a host star, that occurs when the orbit of one of a planet passes in front of the star. Therefore, in order to detect transiting exoplanet, the position between the planetary system and the observer is important, only edge-on planetary system are observed.

2.4.1.1 Transit probability

The probability of having an eclipsing planetary system can be computed from the inclination of the orbit with respect to the observer. The inclination angle (i) and latitude of trajectory (δ) are equivalent;

In order to have a transit we need:

$$h \leq R_* + R_p. \tag{2.2}$$

where h is the projection separation of the planet from the host star at conjunction, R_* and

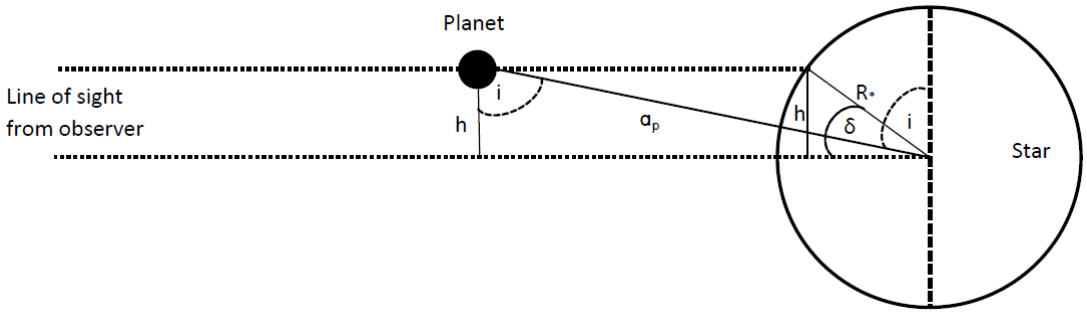

Figure 2.3: Edge-on view.

R_p are the radius of star and planet, respectively. A random distribution will have equally probable values over the range of the angle (i). The geometric transit probability is:

$$P_{tran} = \left(\frac{R_* + R_p}{a_p}\right)\left(\frac{1 + e_p \cos(\pi/2 - \omega_p)}{1 - e_{\rm p}^2}\right). \tag{2.3}$$

where e_p is an orbital eccentricity of the planet and ω_p is a planet argument of periastron (Charbonneau et al., 2007).

2.4.1.2 Transiting exoplanet light curve

The transiting exoplanet light curve is described by the total measured flux of the star and planet,

$$F = F_p + F_* - \begin{cases} 0 & \text{outside eclipses,} \\ F_* \alpha_{tra} & \text{transits,} \\ F_p \alpha_{occ} & \text{occultations,} \end{cases}$$

where F_p and F_* are the fluxes of planet and star, respectively, α is a fraction of area of overlap between planet and star during transit.

The shape of transit dip in transit light curve is described by three main parameter: transit depth, transit duration, and ingress and egress duration. These three parameters depend on the sizes of the planet and the star, the inclination of the planet and their separation (Figure 2.4).

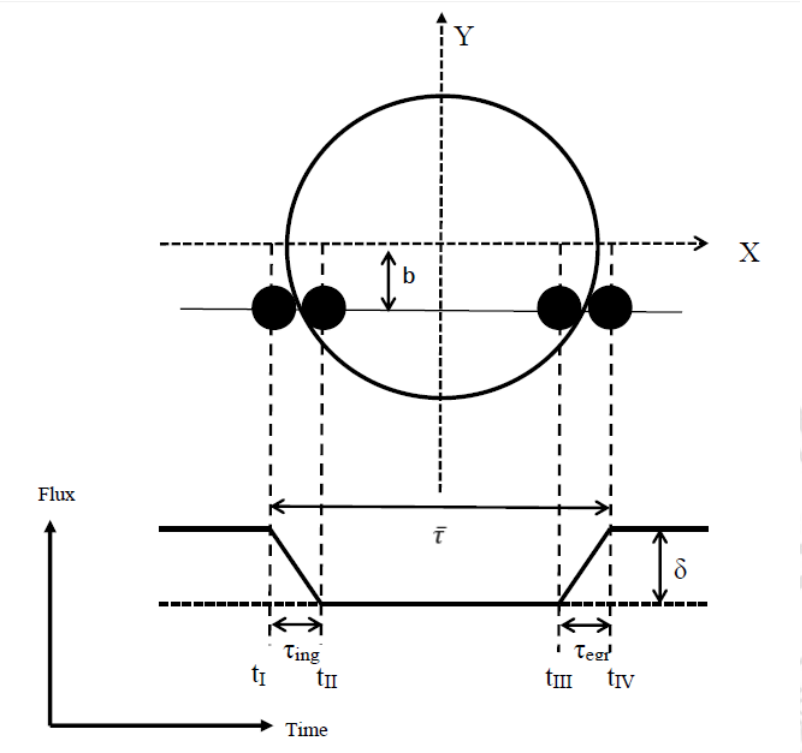

Figure 2.4: Transiting light curve with four contact points.

1. **Transit depth** The relative of the transit depth is given by the ratio of projected area of the planet radius (R_p) and the star (R_*);

$$\delta = \left(\frac{R_p}{R_*}\right)^2 \left(1 + \frac{F_p}{F_*}\right). \tag{2.4}$$

In this case, flux of the star and planet are assumed to be constant, however, the stellar variability might cause significant charge on the transit light curve (Czesla et al. (2009) and Silva (2003)). However, the planetary flux compares with the stellar flux is very faint. Therefore, the planetary flux can be removed,

$$\delta \approx \left(\frac{R_p}{R_*}\right)^2. \tag{2.5}$$

From equation 2.5, the depth of the transit light curve can provide exact radius of the exoplanet.

2. **Transit duration** The transit duration is the duration between the first contact

and the last contact. For a circular orbit, the duration is defined by,

$$\bar{\tau} = t_{IV} - t_I = \frac{P_p}{\pi}\arcsin\left(\sqrt{\frac{1-b^2}{(a_p/R_*)^2 - b^2}}\right). \tag{2.6}$$

where b is an impact parameter (Seager and Mallén-Ornelas, 2003). From Figure 2.4, t_I, t_{II}, t_{III} and t_{IV} are position of first contact, second contact, third contact and last contact, respectively. For an edge-on system ($b = 0$), if the Kepler's third law is applied, the transit duration can be written as,

$$\bar{\tau} = \frac{R_*}{a_p}\frac{P_p}{\pi} = \sqrt[3]{\frac{3}{G\pi^2}\frac{P}{\rho_*}}. \tag{2.7}$$

where ρ_* is the mean density of the star and G is the gravitational constant. Therefore, the duration of transit can be use to estimate the mean stellar density (Perryman and Hainaut (2005) and Seager and Mallén-Ornelas (2003)).

3. **Ingress and egress durations** The shape of the dip is defined by duration of ingress (τ_{ing}) and egress (τ_{egr}), which are the duration between the first and the second contact time and between the third and the fourth contact time, respectively. The ingress and egress are equal in circular orbit,

$$\tau = \tau_{ing} = \tau_{egr} = t_{II} - t_I = t_{IV} - t_{III} = \bar{\tau}\frac{R_p}{R_*}\sqrt{1-b^2}. \tag{2.8}$$

However, τ_{ing} and τ_{egr} are unequal for an eccentric orbit because of the variation in projected speed (Winn, 2010). For edge-on circular system, Southworth et al. (2007) suggests that the transit duration of ingress and egress can be used to estimate surface gravity of the planetary (g_p) by using Kepler's third law and observation of radial velocities, following equation 2.1,

$$\tau = \tau_{ing} = \tau_{egr} = \frac{R_p}{a_p}\frac{P_p}{\pi} = \sqrt{\frac{2}{\pi}\frac{P_p K_*}{g_p}}. \tag{2.9}$$

2.4.1.3 Determining system parameter

The objective of observing transiting exoplanet is to determine parameter of the star and planet. A combination of transit data and radial velocities allows us to fully understand the orbit of the exoplanet and break the degeneracy that are obtained from radial velocity measurements between the mass of the planet and the inclination angle (one can only constrain $M\sin i$ with the radial velocities).

1. **Impact parameter**

Impact parameter (b) is perpendicular distance from the centre of star's disc and the centre of planet's disc. The impact parameter can be written in term of $\bar{\tau}$ and τ, for circular orbit,

$$b^2 = \frac{(1-\frac{R_p}{R_*})^2 - (\frac{\bar{\tau}-2\tau}{\bar{\tau}})^2(1+\frac{R_p}{R_*})^2}{1-(\frac{\bar{\tau}-2\tau}{\bar{\tau}})^2} \ . \tag{2.10}$$

For small planetary system, $\tau \ll \bar{\tau}$, the impact parameter is,

$$b^2 = 1 - \frac{R_p}{R_*}\frac{\bar{\tau}}{\tau} \ . \tag{2.11}$$

2. **Scale stellar radius** The scale stellar radius (R_p/a) is the ratio between the radius of the star and the semi-major axis of the planetary orbit. The scale stellar radius can be written as,

$$\frac{R_*}{a} = \frac{\pi\sqrt{\bar{\tau}\tau - \tau^2}}{P}\sqrt{\frac{R_*}{R_p}}\left(\frac{\sqrt{1+e\sin\omega}}{\sqrt{1-e^2}}\right) . \tag{2.12}$$

For small planetary system, the scale stellar radius is,

$$\frac{R_*}{a} = \frac{\pi\sqrt{\bar{\tau}\tau}}{P}\sqrt{\frac{R_*}{R_p}}\left(\frac{\sqrt{1+e\sin\omega}}{\sqrt{1-e^2}}\right) \ . \tag{2.13}$$

3. **Mean density** The stellar mean density (ρ_*) and planetary mean density (ρ_p) can be determined from the scale stellar radius,

$$\rho_* + \left(\frac{R_p}{R_*}\right)^3\rho_p = \frac{3\pi}{GP^2}\left(\frac{a}{R_*}\right)^3 \ . \tag{2.14}$$

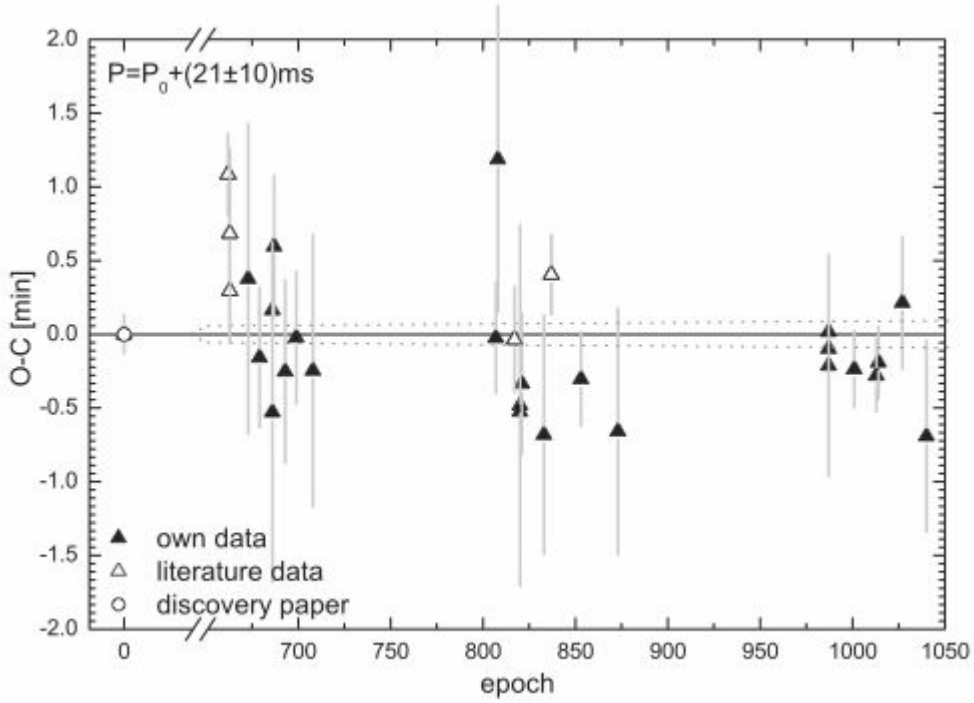

Figure 2.5: The O-C diagram of HAT-P-32 (Seeliger et al., 2014).

Due to the radial ratio of the star and the planet is quite small, the stellar mean density can be obtained from the transit light curve,

$$\rho_* = \frac{3\pi}{GP^2}\left(\frac{a}{R_*}\right)^3 . \tag{2.15}$$

2.4.1.4 O-C diagram

The O-C diagram is a diagnostic tool in natural sciences. Basic period analysis consists of finding a reliable ephemeris of the main periodic variable and modelling of the first order effects. The basic mechanisms of the periodic or nearly periodic stellar variability are the rotation of an anisotropically radiating star, the orbital motions of components in stellar systems, and pulsations or oscillations of various kinds (Mikulášek et al., 2011).

The O-C diagram is a plot showing the observed time of mid transit (O) (for transit exoplanet) or maximum light (for variable star) minus those calculated according to

an adopted ephemeris (C) as a function of time. The horizontal axis of the an O-C diagram most often represent time, usually expressed in days. Scientists principally use the Barycentric Julian Date (BJD) of the observation. Epoch which is the repeating period of observation can also be used. The vertical axis is the "$O - C$" time which gives the diagram its name and its interpretive power. For each observed event one takes the observed time of the event (that's the "O" part) and subtracts the time predicted from the existing data or model of the star. The difference, Observed minus Calculated times or "$O - C$", is plotted on the vertical axis of the graph. The pattern that appears in the O-C diagram can identify if the predictions (or model) are valid.

For a star with no measurable change in the period or in a case of constant period, data on the O-C diagram will scatter approximately as a straight horizontal line across the graph (Figure 2.5). The size of the scatter is an indication of the accuracy of the observed times of maximum. The O-C method, basically, assumes the use of a stable and accurate clock. The credibility of obtained astrophysical information strictly depends on the reliability of observation times and their uncertainties. If the period of the star is changing at a slow constant rate, then a good approximation of the O-C diagram can be represented by a parabola (Figure 2.6). In order to interpret an O-C diagram correctly, a number of cycles, which have elapsed between observed data, should be known. This is not always the case, since there may be large gaps between observations. Other problem is when the period has been changed significantly between observations.

The longer the time interval (in cycles) over which the data have been collected, the higher will be the resulting accuracy of the solution (Sterken, 2005). If the period is slightly increased, the O-C diagram will look like on inclined straight line (Figure 2.7). If the O-C diagram is a curve, the period of the system will slowly change. Therefore the graph with an upward curve, has slowly increasing period (Figure 2.8), while the graph with a downward curve has slowly decreasing period (Figure2.9). For O-C diagram of the system that has third body shown in Figure 2.10, a plot of the residuals around the fit shows a clear deviation from the predicted transit times, meaning that the orbital period of KOI-372b is variate.

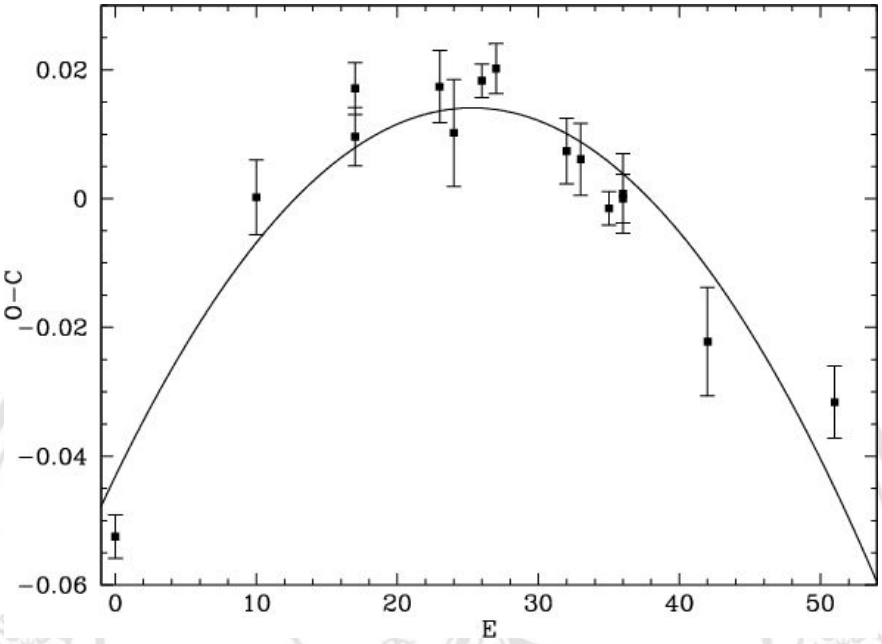

Figure 2.6: The O-C diagram of Var73 Dra (Nogami et al., 2003).

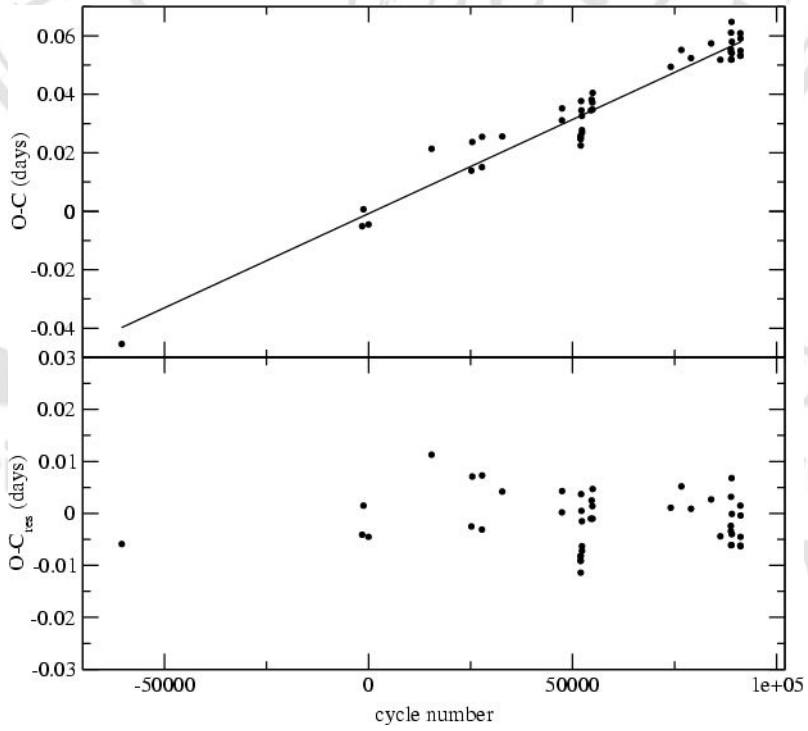

Figure 2.7: The O-C diagram of V567 Oph (Kiss et al., 2002).

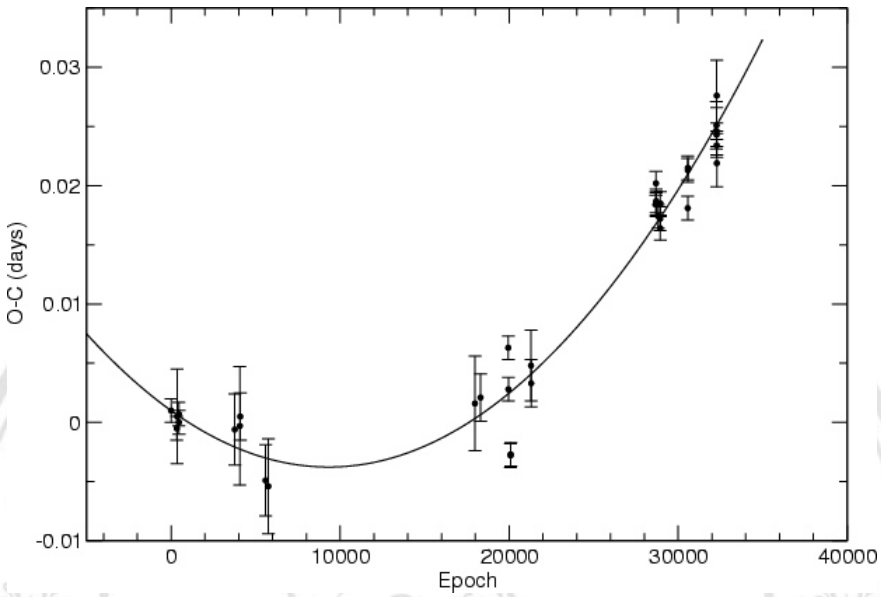

Figure 2.8: The O-C diagram of V617 and to a continuous period increase rate: $dP/dE = +1.1 \times 10^{-10}$ days/year (Steiner et al., 2006).

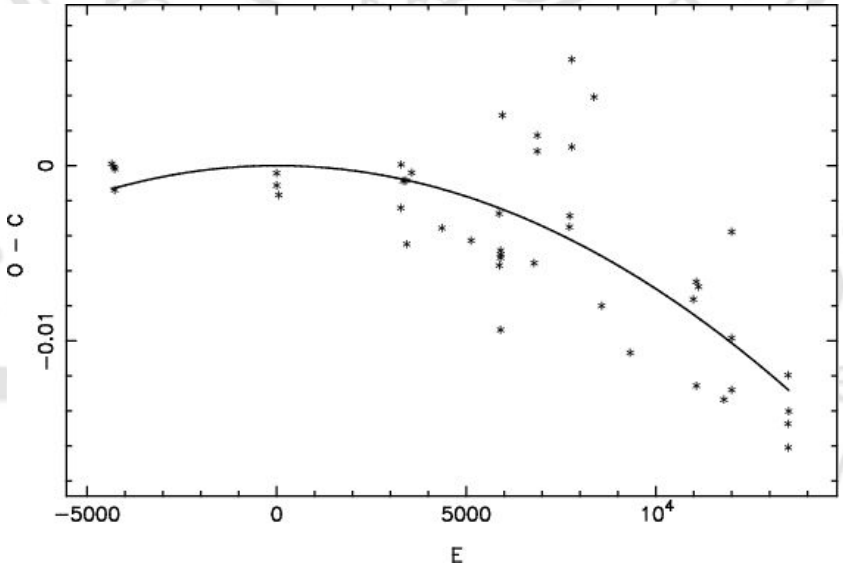

Figure 2.9: The O-C diagram of GR Tau, the rate of the period decreases and turns out to be $\sim$0.01 s.yr^{-1}(Zhang et al., 2002).

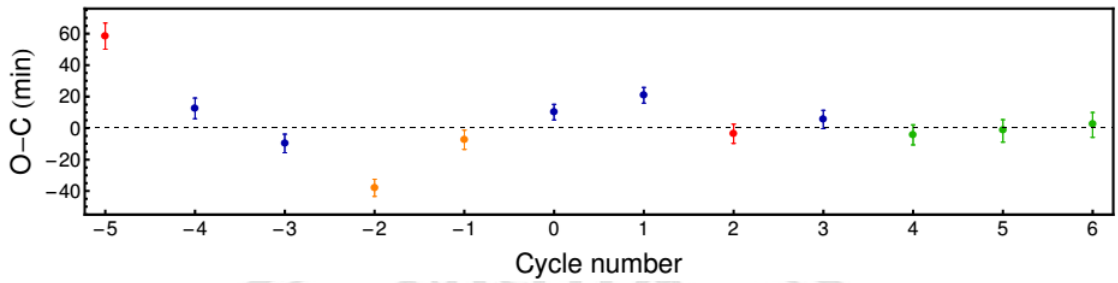

Figure 2.10: O-C diagram for the timings of KOI-372b at mid-transit versus a linear ephemeris (Mancini et al., 2015). The timings in blue refer to those coming from the Kepler long cadence data, while those marked with green are from short cadence data. The red points refer to the two long cadence transits affected by star spots. The two incomplete long cadence transits are marked with orange points.

The appearance of O-C diagram is strongly dependent on the ephemeris formula used to construct it. Analytical procedure for an O-C diagram use basic method as follow. In this section we explain the method for exoplanet observed by transit method with a constant period.

The time of mid transit is given by a linear approximation:

$$T_{mid} = T_0 + P \cdot E \ , \tag{2.16}$$

where T_{mid} is the time of mid transit, T_0 is time of mid transit at the zero epoch, P is the period and E is the number of cycles elapsed since the zero epoch. T_0 and P are obtained through fitting solution.

O-C diagram can be calculated from equation,

$$O - C = T_{mid} - (T_0 + P \cdot E) \cdot \tag{2.17}$$

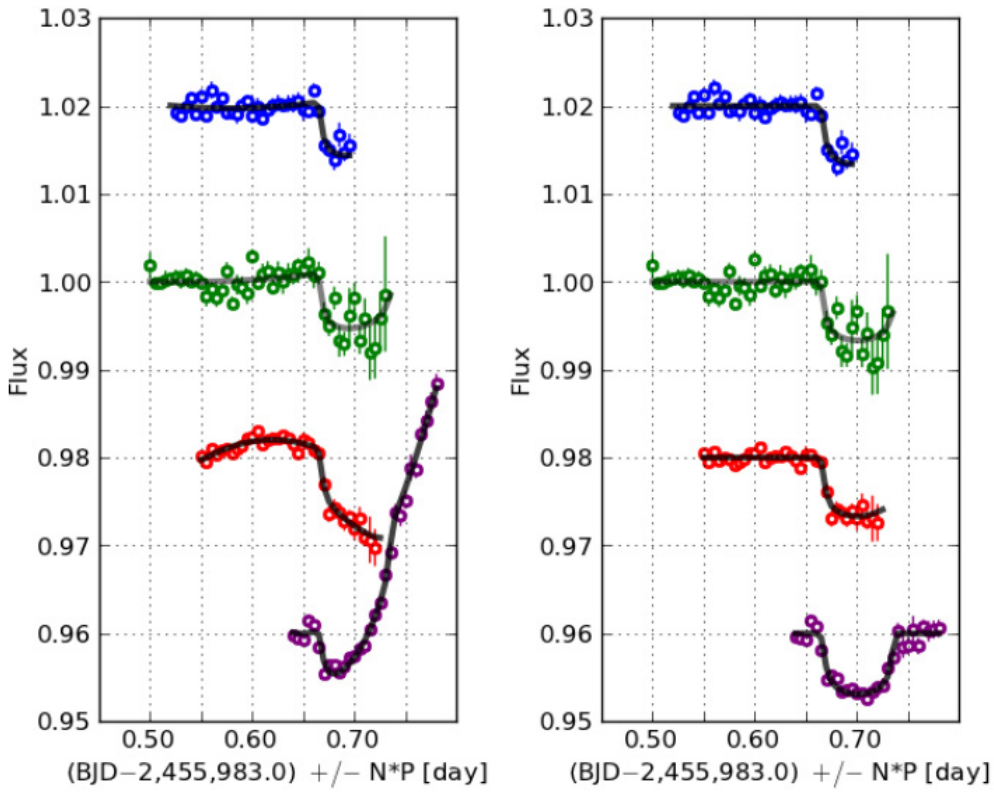

Figure 2.11: Light curves of GJ3470 (Bonfils et al., 2012).

2.5 GJ3470b exoplanet

The exoplanet GJ3470b was discovered by Bonfils et al. (2012). They used spectroscopic detection and photometric observation to detect the planet. For spectroscopic detection, they observed GJ3470 with the HARPS spectrograph; modern velocimeter fiber-fed by the ESO/3.6-m telescope (Mayor et al. (2003) and Pepe et al. (2004)). GJ3470 is part of an extended sample of ∼300 M dwarfs specifically targeted to search for short-period planets, and the subset that transit. They collected 61 radial-velocity observations of GJ3470 between 08 Dec 2008 and 14 Jan 2012. All are 900-s exposures except the first one, which is a 300-s exposure used to verify that the star is suitable for a planet search. For photometric detection, firstly, transit ingress detected with with TRAPPIST and followed by the confirmation with EulerCam, TRAPPIST and NITES.

From figure 2.11, the light curves of GJ3470b is shown. The left panel corresponds

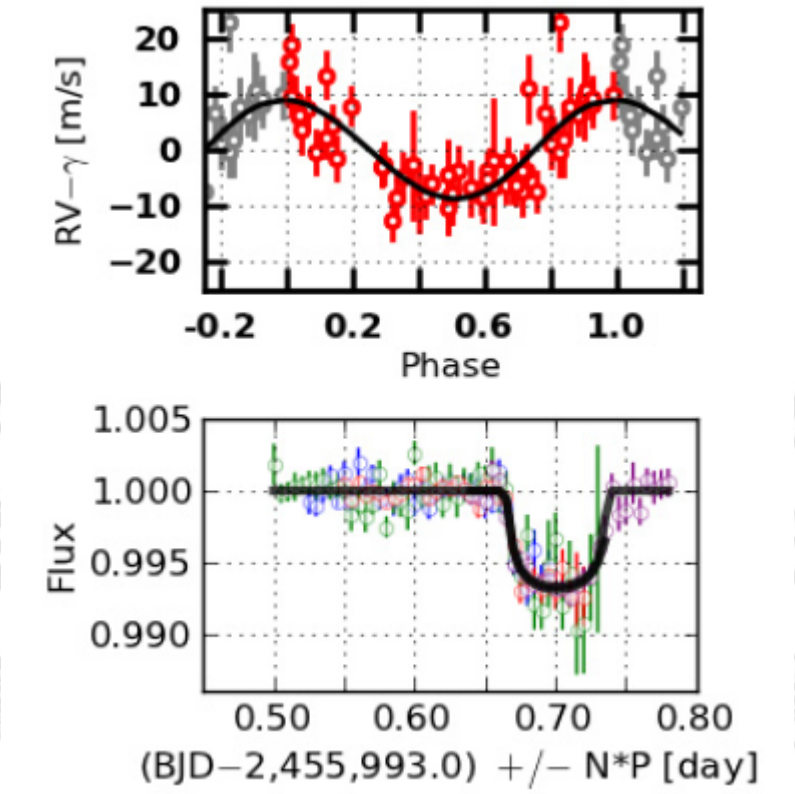

Figure 2.12: RV (*top*) and photometry time series (*bottom*) phased to the planet's orbital period (Bonfils et al., 2012).

to raw light curves (with arbitrary offsets for clarity). The right panel corresponds to detrended light curves. From top to bottom, light curves were obtained with TRAPPIST (on 26 February and 7 March 2012), EulerCam (on 7 March 2012) and Nites (on 12 April 2012). The optimum model is over-plotted with a black curve. To measure physical and orbital parameters of the GJ3470 planetary system, they gather the photometry and radial-velocity time series. The optimal model emerging from their stochastic fitting is shown in Figure 2.12, which it is plotted over the phase-folded RV and photometric data. From these analysis, physical parameters of the planetary system are obtained, i.e., period P = 3.3371±0.0002 day, radius R_p = 4.2±0.6$R_\oplus$, and mass M_p = 14.0±1.8$M_\oplus$. This confirmed that it is a transiting of hot Uranus. Its host star is nearby M1.5 dwarf of mass M_* = 0.054±0.07$M_\odot$ and radius R_* = 0.50±0.06$R_\odot$.

In 2013, There are several researches to studying exoplanet GJ3470b. Demory

et al. (2013) observed two consecutive transits of GJ3470b at 4.5 μm using Spitzer's InfraRed Array Camera (IRAC; (Fazio et al., 2004)). Observations took place on 11 and 15 June 2012 UTC. They supplemented Spitzer photometry with Speckle observations to explore the possibility of blended companions at close angular separations from GJ3470. Speckle observations of GJ3470 were obtained at the WIYN 3.5-m telescope on 2 December 2012. In addition, they observed with a near-infrared spectroscope, on November 2012 with the Folded-port Infrared Echellette (FIRE) spectrograph at the 6.5-m Magellan Baade telescope. They derived a stellar mass to $M_* = 0.539^{+0.047}_{-0.043}\mathrm{M}_\odot$ and a radius to $R_* = 0.568^{+0.037}_{-0.031}\mathrm{R}_\odot$.

From stellar parameter, density of star can be derived to be $\rho_* = 2.91^{+0.37}_{-0.33}\rho_\odot$. The phase-folded Spitzer light curve is shown in Figure 2.13. They determine GJ3470 to be metal-rich, with a metallicity of [Fe/H] = +0.20 $\pm$ 0.10 and an effective temperature of T_{eff} = 3600 $\pm$ 100K. The revised stellar parameters yield a planetary radius $R_p = 4.83^{+0.22}_{-0.21}\mathrm{R}_\oplus$ that is 13% larger than the value previously reported in the literature. They found mass $M_p = 13.9^{+1.5}_{-1.4}\mathrm{M}_\oplus$ that translates to a very low planetary density, $\rho_p = 0.72^{+0.13}_{-0.12}$ g.cm^{-3}.

Next, Fukui et al. (2013) presented optical (g', R_c, and I_c) to near-infrared (J) simultaneous photometric observations for a primary transit of GJ3470b, by used the 0.5-m MITSuME telescope and the 1.88-m telescope, both at the Okayama Astrophysical Observatory. In Figure 2.14 shows the baseline-corrected J-band light curve and the derived model light curve for the respective bands are shown in Figure 2.15.

From data observation and analysis, they derived the planetary mass, radius and density as $M_p = 14.1\pm1.3\mathrm{M}_\oplus$, $R_p = 4.32^{+0.21}_{-0.10}\mathrm{R}_\oplus$, and $\rho_p = 0.94\pm0.12$ g.cm^{-3}. They found that the planet-to-star ratio (R_p/R_*) in J band ($0.07577^{+0.00072}_{-0.00075}$) is smaller than that in the I_c (0.0802$\pm$0.0013) and 4.5 μm ($0.07806^{+0.00052}_{-0.00054}$) bands by 5.8% $\pm$ 2.0% and 2.9% $\pm$ 1.1%, respectively. A plausible explanation for the differences is that the planetary atmospheric opacity varies with wavelength due to absorption and/or scattering by atmospheric molecules. Although the significance of the observed R_p/R_* variations is low, if confirmed, this fact would suggest that GJ3470b does not have a thick cloud layer in the atmosphere.

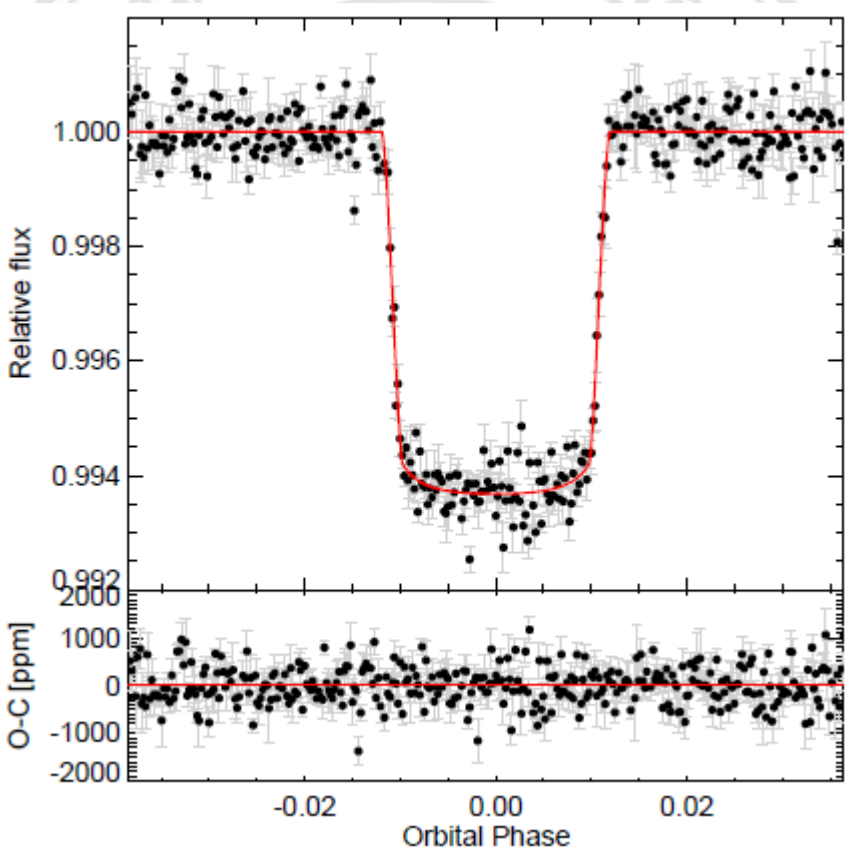

Figure 2.13: The light curve of GJ3470b from $Spitzer$/IRAC 4.5 μm photometry with the best-fit transit model ($Top\ panel$) and the residual light curve ($Bottom\ pamel$) (Demory et al., 2013).

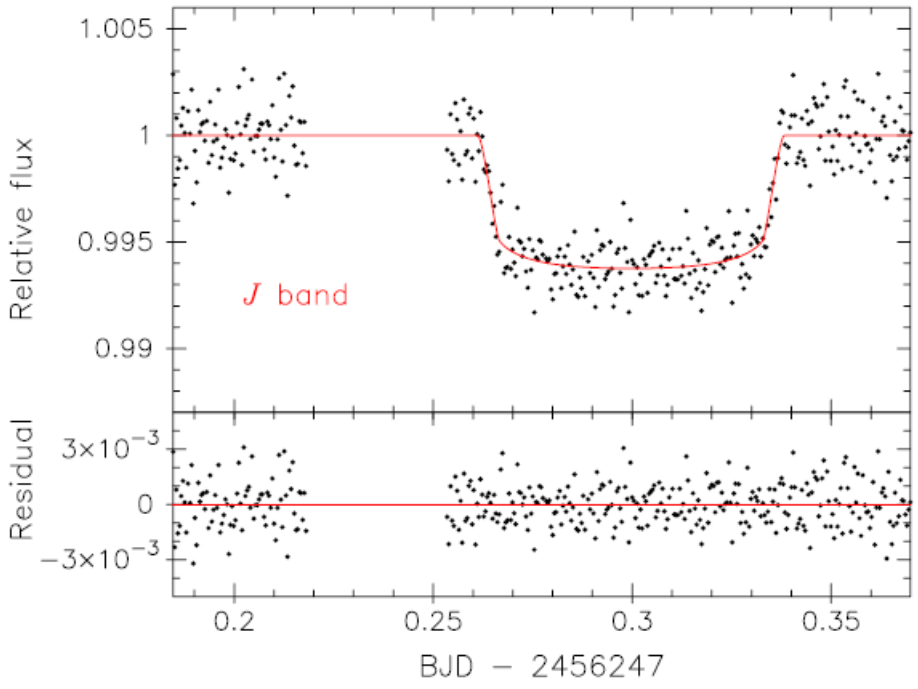

Figure 2.14: The baseline-corrected J-band light curve ($Top\ panel$) and the residual light curve ($Bottom\ pamel$) (Fukui et al., 2013).

Nascimbeni et al. (2013) presented two new ground-based light curves of GJ3470b by the LBC (Large Binocular Camera) camera at the Large Binocular Telescope. Simultaneous photometry in the U_{spec} filter on the blue channel (centered at λ_c=357.5 nm) and the $F972N20$ filter in the red channel (centered at λ_c=963.5 nm) were conducted. Both sets of frames were bias-corrected and flat-fielded using standard procedures and twilight master flat. Then, they obtained the U_{spec} and $F972N20$ light curves of GJ3470 using STARSKY (STARSKY is a photometric pipeline optimized to perform high-precision differential aperture photometry over defocused images), the two light curves (Figure 2.16 and Figure 2.17) are simultaneous.

Nascimbeni et al. (2013) examine the transmission spectrum of GJ3470b reconstructed by the LBC measurements and from those by Demory et al. (2013) and Fukui et al. (2013) (Figure 2.18). From data analysis of Nascimbeni et al. (2013) with Demory et al. (2013) and Fukui et al. (2013), it can be interpreted as a signature of scattering processes occurring in the planetary atmosphere, which should be cloud-free and with a low mean molecular weight. The unprecedented accuracy of their measurements demonstrates

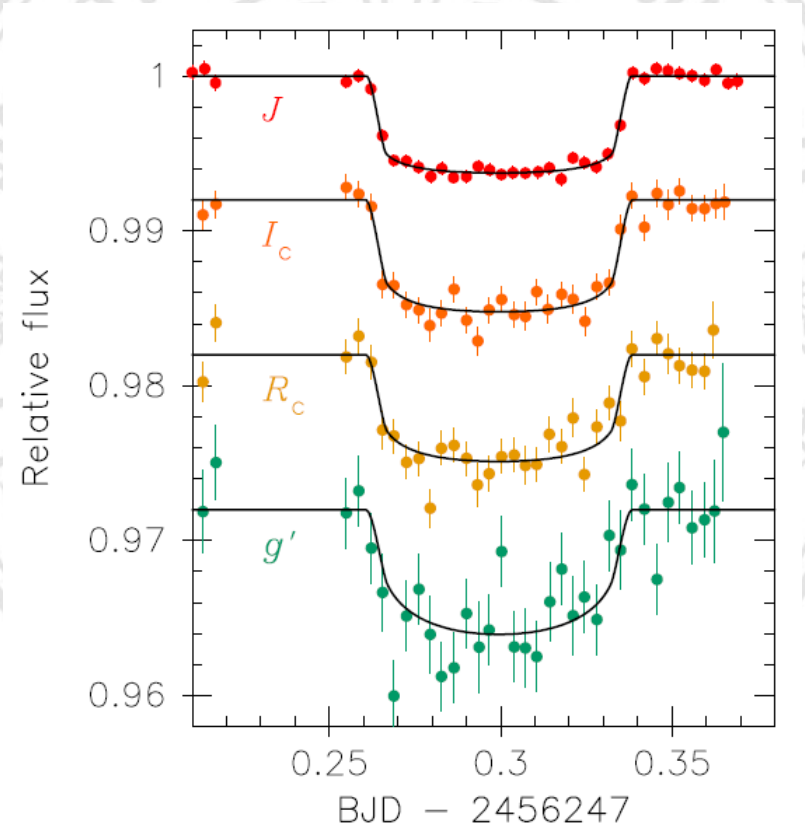

Figure 2.15: The J-, I_c-, R_c-, and g'-band light curves after the baseline correction and five minute binning (Fukui et al., 2013).

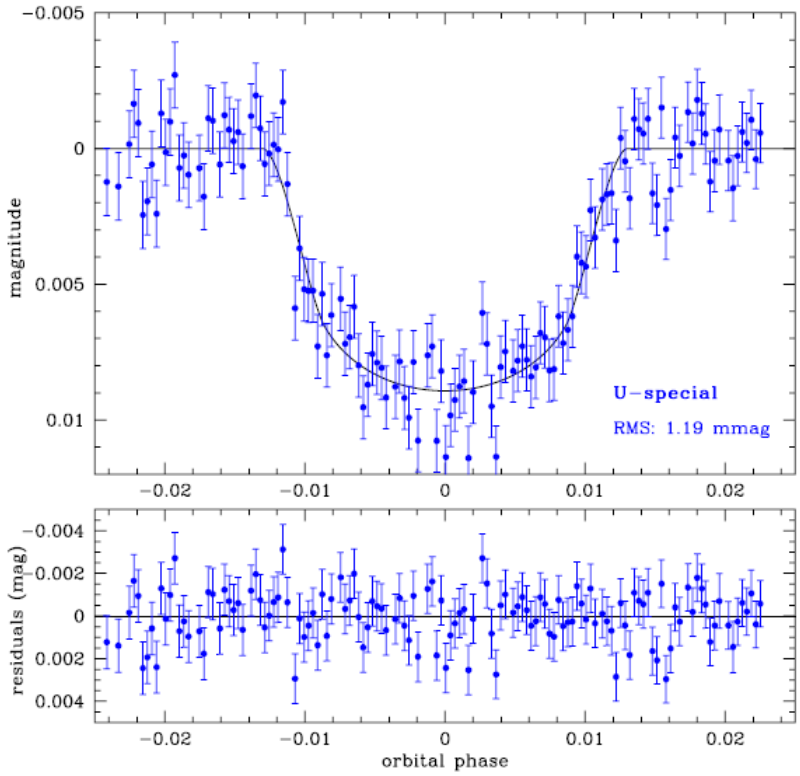

Figure 2.16: Light curve of GJ3470b with the U_{spec} band (Nascimbeni et al., 2013).

that the photometric detection of Earth-sized planets around M-dwarfs is achievable using 8-10 m size ground-based telescopes. They updated planetary parameters are period P_p = 3.336649±0.000002 day, radius $R_p = 0.07484^{+0.00052}_{-0.00043}R_*$ (LBC $F972N20$) and R_p = 0.0821±0.0013R$_*$ (LBC U_{spec}).

In the same year, Crossfield et al. (2013) reported their spectroscopic investigation of the transiting ice giant GJ3470b's atmospheric transmission, with the first results of exoplanet observations from the new Keck/MOSFIRE spectrograph. Figure 2.19 shows the MOSFIRE (Multi-Object spectrometer for Infra-Red Exploration) light curves. They measure a planet/star radius ratio as $0.0789^{+0.0021}_{-0.0019}$. When combined with existing broadband photometry, these measurements rule out cloud-free atmospheres in chemical equilibrium assuming either solar abundances or a moderate level of metal enrichment, confirming previous results that such models are not representative for cool, low-mass, externally irradiated extrasolar planets. The measurements of this research are consistent with a flat transmission spectrum, which suggests that the atmosphere is explained by high- altitude

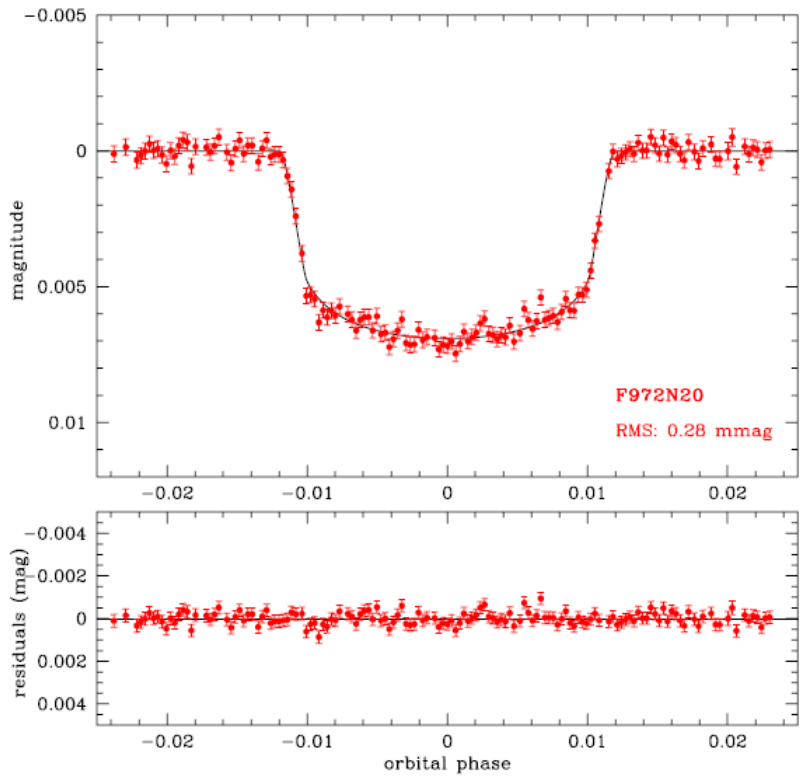

Figure 2.17: Light curve of GJ3470b with the $F972N20$ band (Nascimbeni et al., 2013).

clouds and haze, disequilibrium chemistry, unexpected abundance patterns, or the atmosphere is extremely metal-rich.

Later year, Biddle et al. (2014) studied GJ3470 by spectroscopic and photometric techniques. They also collected previously published data, provides improved parameters for the GJ3470 system and a consistency in the analysis process. From spectroscopic measurements of GJ3470, they found R_* = 0.48±0.04R$_\odot$, M_* = 0.51±0.06M$_\odot$ and T_{eff} = 3652±50K, along with a rotation period of 20.70±0.15 day and an R-band amplitude of 0.01 mag. They collected a light curve previously analyzed by Bonfils et al. (2012), Fukui et al. (2013), and Nascimbeni et al. (2013) for a total of 21 light curves plotted in Figure 2.20. They derived a new set of planetary parameters M_p = 13.73±1.61M$_\oplus$, R_p = 3.88±0.32R$_\oplus$ and ρ_p = 1.18±0.33 g.cm^{-3}. They also present the most precise new transit ephemeris for this system and find an updated period of $3.33664874^{+0.0000043}_{-0.0000033}$ day. In addition, they plot the epoch of each transit against the observed time minus the calculated time ($O-C$) in Figure 2.21.

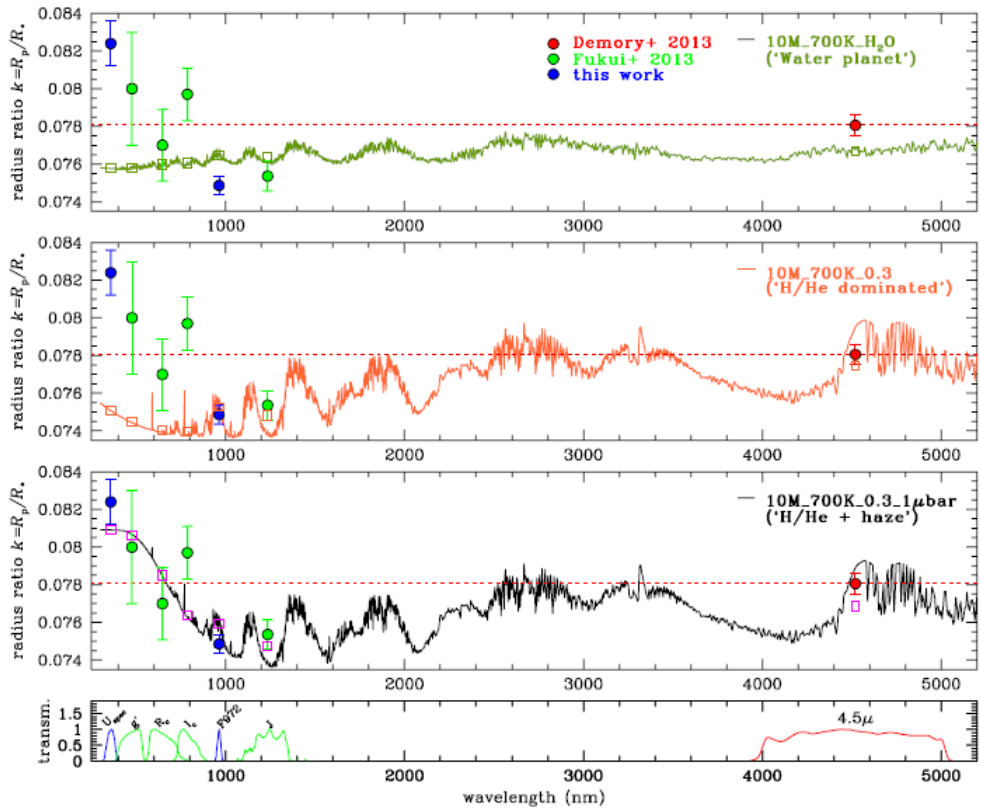

Figure 2.18: The transmission spectrum of GJ3470b, the data from Nascimbeni et al. (2013), Fukui et al. (2013) and Demory et al. (2013). *Upper panel*: the data was fit to Howe and Burrows (2012) model, high mean molecular weight (μ). *Second panel*: same as above, but consider that low mean molecular weight and H/He domineted. *Third panel*: same as above, but adding the contribution of a scattering haze at 1 μbar. *Lower panel*: instrumental passbands employed for each data point (Nascimbeni et al., 2013).

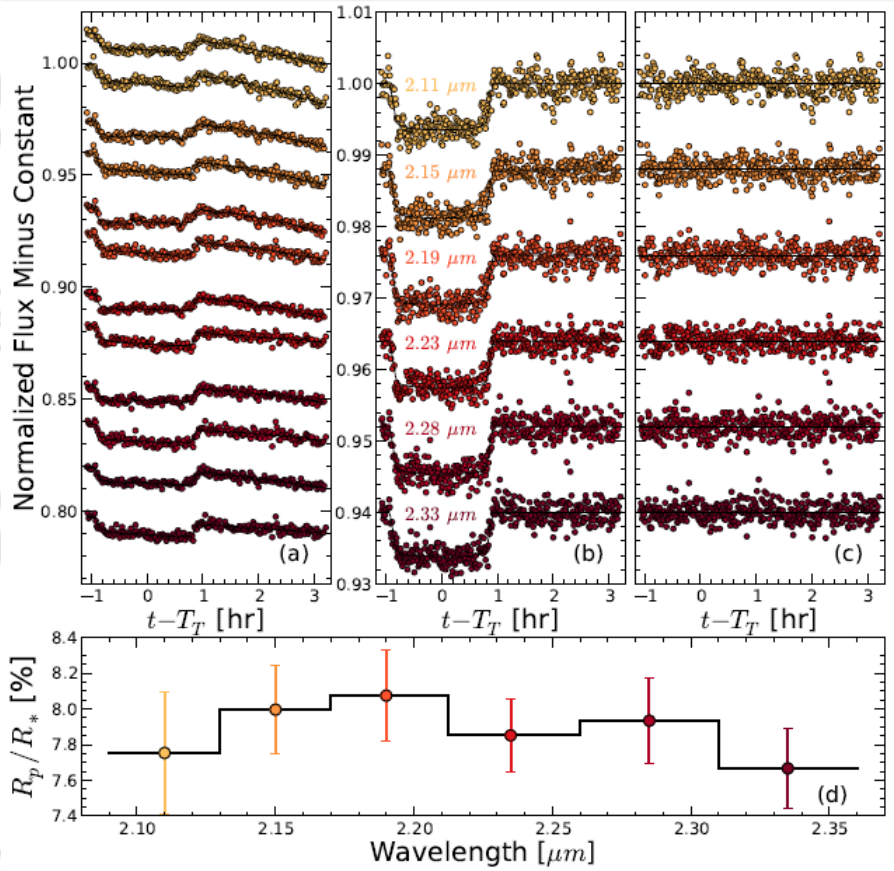

Figure 2.19: The MOSFIRE (Multi-Object spectrometer for Infra-Red Exploration) light curves, best fit model, and residuals to the fit (Crossfield et al., 2013).

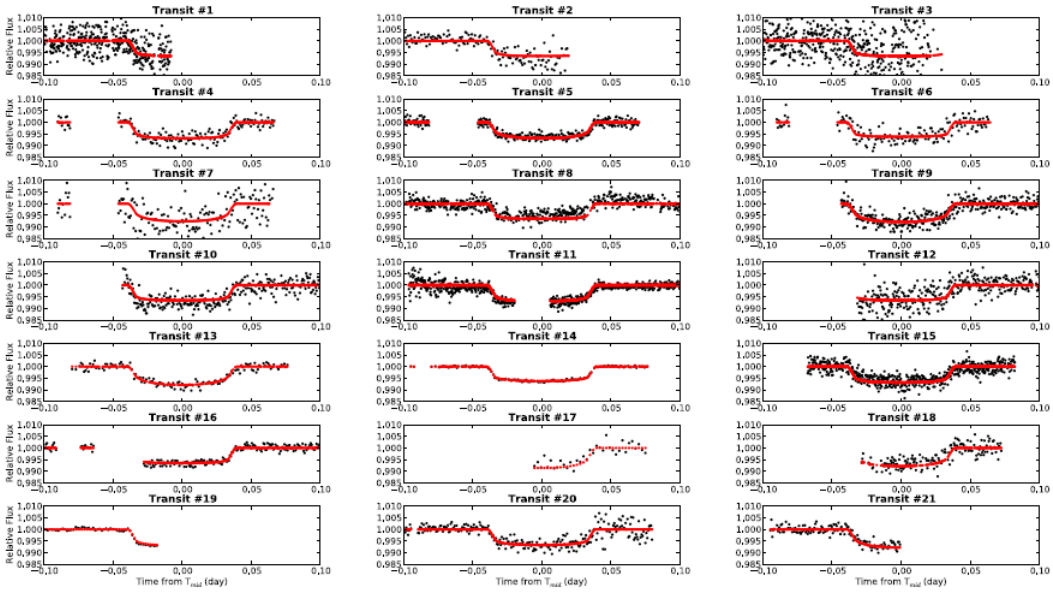

Figure 2.20: The 21 transit light curves of GJ3470b, 12 transit light curves from Biddle et al. (2014), 3 transit light curves from Bonfils et al. (2012), 4 transit light curves from Fukui et al. (2013) and 2 transit light curves from Nascimbeni et al. (2013) (Biddle et al., 2014).

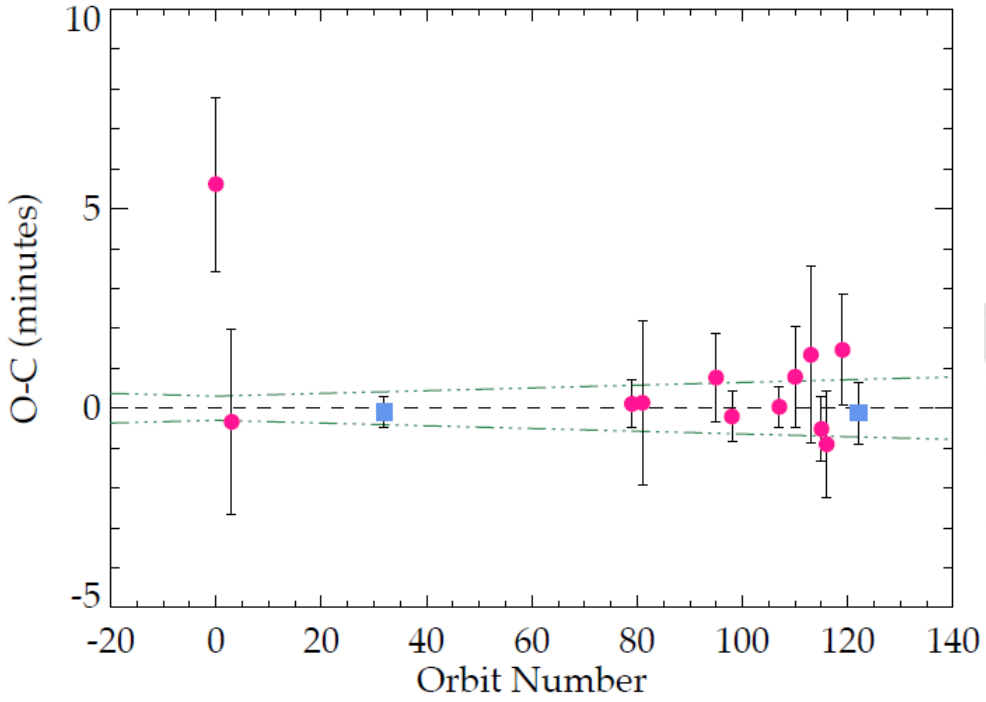

Figure 2.21: O-C diagram of GJ3470b from Biddle et al. (2014).

In the same year, Ehrenreich et al. (2014) presented new simultaneous of possible theoretical transmission spectra for GJ3470b. They observed one transit with the Wide Field Camera-3 (WFC3) on the Hubble Space Telescope. Figure 2.22 (*top*) shows raw white light curve of GJ3470. The raw white light curve was affected by systemic effect, among which the most dominant is a rapid flux increase at the beginning of each batch of exposures. From data analysis, the best fit to the white light curve obtained is shown in Figure 2.22 (*bottom*). The planet-to-star radius ratio is R_p/R_* = (7.848±0.037)%. The broad-band radius ratio corresponding to the WFC3/G141 band pass and derived from their measurements is in agreement (1.4σ) with and similar precision to the photometric value of $(7.798^{+0.046}_{-0.045})$% obtained with Spitzer (Demory et al., 2013). Adopting the stellar radius of R_* = 0.568±0.037 derived by these authors, they found that GJ3470b has a near-infrared radius of R_p = 4.86±0.32R_* (Ehrenreich et al., 2014). They studied planetary atmosphere by using transmission spectroscopy. From the result, they found that a cloudy, hydrogen-rich atmosphere can explain the full transmission spectrum.

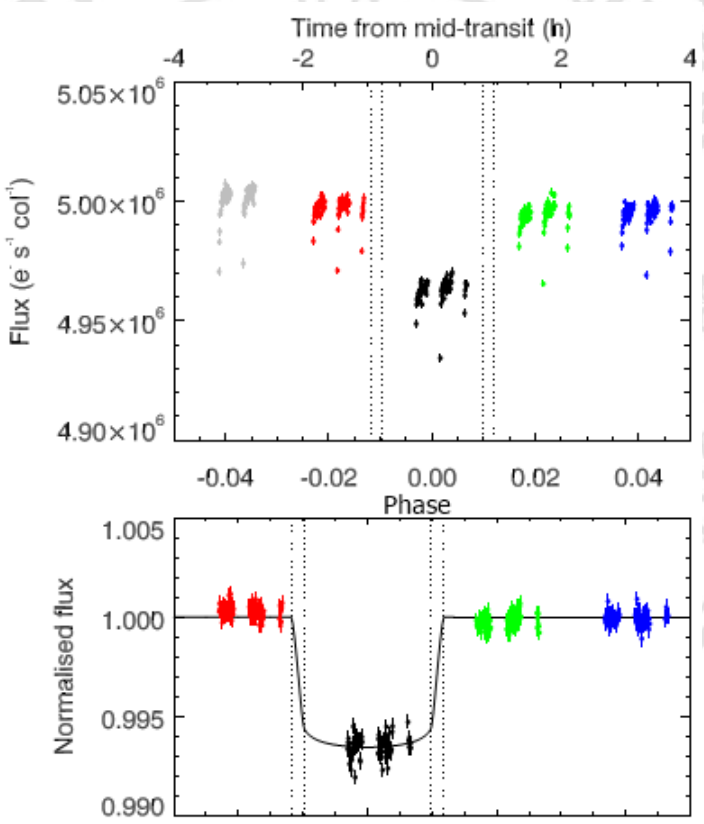

Figure 2.22: *Top panel*:Raw white light curve of GJ3470. *Bottom panel*: Corrected white light curve (Ehrenreich et al., 2014).